International Journal of Remote Sensing
Vol. 00, No. 00, 00 Month 201X, 1–21

regular paper

Detection of environmental hazards through the feature-based fusion of optical and SAR data: a case study in southern Italy

Angela Errico[a], Cesario Vincenzo Angelino[a], Luca Cicala[a], Giuseppe Persechino[a], Claudia Ferrara[b], Massimiliano Lega[b], Andrea Vallario[c], Claudio Parente[c], Giuseppe Masi[d,e], Raffaele Gaetano[d,e], Giuseppe Scarpa[d,e], Donato Amitrano[d], Giuseppe Ruello[d], Luisa Verdoliva[d,e], and Giovanni Poggi[d,e] *

[a] *CIRA, the Italian Aerospace Research Center, Capua, Italy*;
[b] *Department of Engineering, University Parthenope of Naples, Italy*;
[c] *Department of Sciences and Technologies, University Parthenope of Naples, Italy*;
[d] *DIETI, University Federico II of Naples, Italy*;
[e] *CNIT, National Inter-University Consortium for Telecommunications, Italy*;

(*Received 00 Month 201X; final version received 00 Month 201X*)

The use of remote-sensing images is becoming common practice in the fight against environmental crimes. However, the challenge of exploiting the complementary information provided by radar and optical data, and by more conventional sources encoded in geographic information systems, is still open. In this work, we propose a new workflow for the detection of potentially hazardous cattle-breeding facilities, exploiting both synthetic aperture radar and optical multitemporal data together with geospatial analyses in the geographic information system environment. The data fusion is performed at a feature-based level. Experiments on data available for the area of Caserta, in southern Italy, show that the proposed technique provides very high detection capability, up to 95%, with a very low false alarm rate. A fast and easy-to-use system has been realized based on this approach, which is a useful tool in the hand of agencies engaged in the protection of territory.

Keywords: Multisensor data fusion, synthetic aperture radar, GIS, image analysis, environmental hazard detection, digital image forensics.

1. Introduction

Enforcement of environmental regulation is a persistent challenge, and timely detection of violations is key to holding violators accountable. Typically, the investigation is triggered by the evidence of the damage, rather than of the illegal polluting act. Often, the effects appear a long time after the polluting act has been committed, and in a different place. The correlation between the source and the damage depends upon the morphology of the scenario and the physical phenomena that allow the transport of the pollutants (Lega et al. 2012a). In these cases, the effectiveness of investigations can be greatly enhanced by using remote-sensing data and information technology tools. Continuous and targeted monitoring allows for efficient police action (Lega and Napoli 2010; Pringle et al. 2012). Successful identification and prosecution of culprits requires an integrated system based on

*Corresponding author. email: poggi@unina.it

data from several sources, including space, air, waterways, and land monitoring (Lega et al. 2012b).

Environmental monitoring and analysis - and in particular the detection and monitoring of environmental crimes - can produce complex data that are difficult to represent. For these purposes, the use of geographic information systems (GISs) is often considered (Weng 2002; Gao et al. 2013). Its potential has enormously increased, in recent years, also thanks to the availability of a large body of remote-sensing imagery in both optical and radar modalities. The problem has been addressed before in the scientific literature: see, for example, the review papers of Pohl and Genderen (1998) and Zhang (2010). aimed at improving the accuracy of image classification, object recognition, change detection and 3D reconstruction. In particular, some approaches have been proposed that try to integrate data characterized by different data structures, spatial resolution, and geometric characteristics, such as vector data layers, and optical and synthetic aperture radar (SAR) images (Solberg, Taxt, and Jain 1996; Weis et al. 2005; Waske and van der Linden 2008).

With reference to environmental crimes a first step in this direction is found in (Brilis et al. 2001) where information provided by a ground positioning system (GPS) are integrated in a GIS to analyze the source, extent and transport of contaminants. More recent papers rely heavily, and in various ways, on remote sensing imagery. Silvestri and Omri (2008) proposed a method for the identification of uncontrolled landfill by means of multiresolution Ikonos data. In Jensen et al. (2009) a GIS-assisted system for hazardous waste site monitoring, based on the integration of multispectral and lidar data with numerous types of thematic information, is proposed. Slonecker et al. (2010) reviewed the literature of remote sensing and overhead imaging in the context of hazardous waste and discusses future trends with special attention to multispectral and hyperspectral remote sensing data. Faisal, Alahmad, and Shake (2012) and Lein (2013) demonstrate the potential of multi-temporal Landsat images for landfill site monitoring. Im et al. (2007) uses hyperspectral images to characterize vegetation at hazardous waste sites, with different analysis methods (vegetation indices, red-edge positioning, and machine learning).

In parallel with optical remote sensing, research on the use of radar remote sensing data for environmental crimes has also been conducted, with several papers (Ottavianelli et al. 2005; Karathanassi, Choussiafis, and Grammatikou 2012) focusing on the use of SAR interferometry for the detection and monitoring of landfill. In all these papers, interesting cues for future developments are proposed, concerning in particular the integration of various types of information.

In this paper we propose a methodology, using optical and SAR remote sensing data, together with more conventional sources, for the detection of small cattle-breeding areas, potentially responsible of hazardous littering. Starting from the analysis of a small number of companies already surveyed or known a priori, we extract a general description of some typical features of such facilities, and of their signatures in remote sensed imagery, both optical and SAR. This information is then used in a geospatial data-processing workflow to detect new facilities of the same type unknown according to the official census. Experiments on a test area, with available specific ground truth, prove that the proposed system is characterized by very large detection probability and a negligible false alarm rate. The research, carried out in the context of a large regional project (Persechino et al. 2013) aimed at contrasting environmental crime, benefited from continuous interaction with various institutions and gathered a variety of complementary scientific

skills, leading to the implementation of an efficient and user-friendly software tool.

A typical buffalo-breeding facility in Campania, Italy, is characterized by one or more rectangular sheds with metal cladding. The terrain adjacent to such structures is divided into spaces available for the animal manger and fenced areas where buffalo spend most of the day. Sometimes these large enclosures contain artificial lakes and canopies to protect the animals from the summer heat. Often, another space or tank is dedicated to the accumulation and deposition of heaps of manure. Of course, several deviations from this "typical" structure can be found: sometimes the sheds are relatively far from the fenced areas and can have more complex geometries, roofs can be made of a different material, etc. The available administrative data concern the initial registrations of new buffalo-breeding facilities (BBFs) on the productive activity register in the province of Caserta. The official headquarters of the company is usually (but not always) located near the facilities.

2. The case study: detection of small buffalo breeding facilities

In this section, we present the case study: the detection of hazards with reference to BBFs. Also, we describe the available data sources, both optical and SAR, acquired in the province of Caserta.

2.1 *Environmental hazards related to buffalo breeding*

Pollutants from manure, litter, and process wastewater can seriously affect human health and the environment (Horrigan, Lawrence, and Walker 2002; Menzi et al. 2010; Fatta-Kassinosa et al. 2011). Whether from poultry, cattle, or swine, these contain substantial amounts of nutrients (nitrogen, phosphorus, and potassium), pathogens, heavy metals, and smaller amounts of other elements and pharmaceuticals (Gerba and Smith 2005). This material is commonly applied to crops associated with concentrated animal feeding operations (CAFOs) or transferred off site. Whether over-applied or applied before precipitation events, excess nutrients can flow from agricultural fields, causing harmful aquatic plant growth, commonly referred to as algal bloom, which can cause fish death and contribute to dead zones. In addition, algal bloom often releases toxins that are harmful to human health.

More than 40 diseases found in manure can be transferred to humans, including the causative agents of salmonellosis, tuberculosis, and leptospirosis. Exposure to waterborne pathogen contaminants can result from both recreational use of affected surface water (accidental ingestion of contaminated water and dermal contact during swimming) and ingestion of drinking water derived from either contaminated surface water or groundwater. Heavy metals such as arsenic, cadmium, iron, lead, manganese, and nickel are commonly found in CAFO manure, litter, and process wastewater (Jongbloed and Lenis 1998). Some heavy metals, such as copper and zinc, are essential nutrients for animal growth, especially for cattle, swine, and poultry. However, farm animals excrete excess heavy metals in their manure, which in turn is spread as fertilizer, causing potential run-off problems.

To promote growth and to control the spread of disease, antibiotics, growth hormones, and other pharmaceutical agents are often added to feed rations or water, directly injected into animals, or administered via ear implants or tags. Most antibiotics are not metabolized completely and are excreted from the treated animal shortly after medication. As much as 80-90% of some administered antibiotics

occur as parent compounds in animal wastes. Steroid hormones are of particular concern because there is laboratory evidence that very low concentrations of these chemicals can adversely affect the reproduction of fish and other aquatic species. The dosing of livestock animals with antimicrobial agents for growth promotion and prophylaxis may promote antimicrobial resistance in pathogens, increasing the severity of disease and limiting treatment options for diseased individuals (EPA 2011).

2.2 *Buffalo breeding facilities in the province of Caserta*

This specific environmental problem is very relevant for the Caserta area in southern Italy, which therefore represents an interesting case study (Infascelli et al. 2010). Caserta is the northernmost province of Campania, one of the most densely populated regions of Italy, and among the poorest. Campania is an agricultural region, very productive and highly specialized, with a model of extensive cultivation. Nearly 80% of farm work is carried out on family farms, so agricultural production units are very small (3.6 ha on average). Mainly fruit and vegetables are produced, but buffalo breeding for mozzarella production is also important. In fact, the Caserta area is one of the main production sites of the "Mozzarella di Bufala Campana", the world-famous fresh cheese holding the status of a protected designation of origin under the European Union. In 2006 Campania produced 34,000 t of mozzarella, about 80% of national production.

The food production system in Italy, and especially in Campania, is relatively vulnerable to waste contamination (Barba et al. 2011). Sometimes, this is due to the massive level of crime perpetrated by large-scale criminal organizations, but also it is the result of a culture of illegal practices and neglect widespread among small farm owners (Esposito et al. 2010; Triassi et al. 2015).

Concerning BBF, in particular, besides many technologically advanced and lawabiding companies, many small factories exist which are not even on the productive activity register, and are not easily monitored or surveyed. Awareness of this problematic issue has been raised by many recent cases of pollution due to illicit spills involving BBFs. These cases have been reported in the course of inspections carried out by forestry personnel in collaboration with the local agencies in Campania. In particular, these investigations have made it clear that some holders did not properly accumulate and download all heaps of manure, with several cubic metres having been downloaded over a few square metres. This is in open violation of the established specific rules on how wastewater can be spread on soils. Manure cannot be accumulated in a small area as this represents a serious source of pollution. This is a bad habit that becomes a serious danger when BBFs are located in proximity to rivers, archaeological areas, or urban centres.

2.3 *Available data*

2.3.1 Optical images

Two multiresolution optical images have been used in this work, acquired by the GeoEye sensor on 2010-07-29 and 2011-08-12, which cover a region of about 20 $\times$ 16 km^2 in the province of Caserta. Although other images were available, we considered only these two, acquired at about the same time of the year, in order to carry out a reliable multitemporal analysis. Each image comprises a panchromatic band with geometric resolution of 0.5 m/pixel, and a 4-band multispectral image

Figure 1. RGB composite of one of the available optical images. The area is about 14 × 12 km^2 with a spatial resolution of 2 m/pixel for the multispectral bands and 0.5 m/pixel for the panchromatic band.

(Blue, Green, Red, Near-Infrared) co-registered with the panchromatic band but with a geometric resolution of 2 m/pixel. Radiometric resolution is 8 bits for all data. Figure 1 shows the RGB composite of the 2010-07-29 image.

2.3.2 SAR images

A set of 15 COSMO-SkyMed single-look complex balanced stripmap SAR images is available for the project, unevenly spanning a temporal interval of two years, between December 14, 2009, and October 17, 2011. All the data are HH polarized, acquired with ascending orbit and look angle of approximately 33^o. The data cover an area of about 40 × 40 km^2, with 3 m/pixel spatial resolution (both in range and azimuth). A calibration set for correcting the effects related to the sensor and the acquisition geometry can be extracted from the ancillary data provided by the Italian Space Agency (ASI). In such way, the achievable radiometric accuracy is about 1 dB. A cut of 5200 × 4600 pixels was used for the proposed project, covering an area of about 195 km^2. Figure 2 shows one of the available SAR images, geocoded and resampled on a map grid of 0.5 m/pixel (for comparison with the pansharpened optical image) after the application of the multitemporal De Grandi filter (De Grandi et al. 1997), followed by a spatial non-local filter (Parrilli et al. 2012). Multitemporal filtering, by exploiting time diversity, helps in reducing speckle and hence improves the performance of the successive segmentation step (Gaetano et al. 2014a). In particular, the De Grandi filter is relatively simple and has proved very effective in the context of several different applications (Ali et al. 2013; Amitrano et al. 2014; Fontanelli et al. 2014). The subsequent non-local filter exploits spatial dependencies to further reduce speckle, while preserving relevant image structures, as shown in Deledalle et al. (2014).

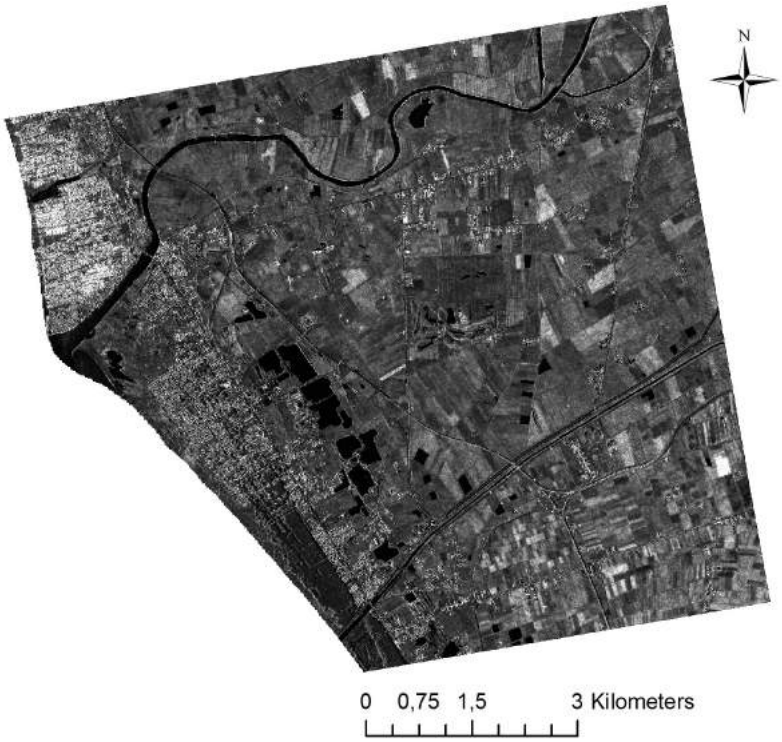

Figure 2. One of the available SAR images in amplitude format. The area is about 14 × 12 km^2 with a spatial resolution of 3 m/pixel.

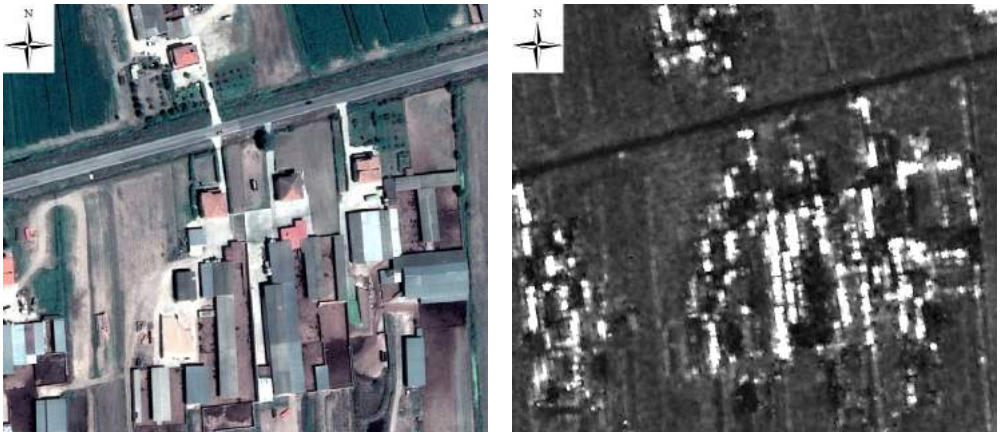

Figure 3. Optical (RGB) and SAR (amplitude) images of a selected region of interest (about 337 × 226 m^2) with several BBFs.

3. Proposed approach

There are probably many ways to combine and exploit the available data to detect small BBFs. In the following, we describe a simple processing chain, based on some preliminary observations on the characteristics of these facilities.

As recorded from the satellite, see Figure 3, BBFs are mainly characterized by the adjacent sheds and fenced uncovered spaces used for both breeding the buffalo and accumulating animal waste. Sheds are clearly visible in both optical images, where they have a saturated response due to their high reflectivity, and the SAR images, where they contribute bright lines due to double-reflection mechanisms. However, these responses are not at all specific and can be confused with other highly reflective covers in the optical images (e.g. bitumenized roads) and, espe-

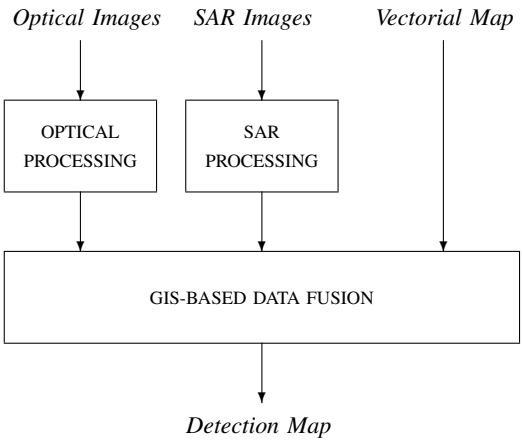

Figure 4. High-level processing chain.

cially, with generic buildings in both sources. Moreover, as mentioned above, sheds are not always close to the fenced spaces where the buffalo live. Conversely, the spectral signature of the manure is highly characteristic, easily discriminated from bare ground in the NIR band, and stable to changes in solar illumination. Needless to say, manure is always present and abundant where the animals live, and indoor breeding is not an acceptable option in the highly standardized buffalo-breeding protocol for the "Mozzarella di Bufala Campana" industry. Therefore, we decided to use GeoEye-1 optical images as main source of information, focusing on the manure signature.

In SAR images, manure does not exhibit a distinctive backscatter. However, we use the SAR stack to detect and mask built-up areas, thus reducing false alarms. This is especially valuable since most false alarms are related to shadows projected by buildings over bare soil, which abound in urban areas due to the high density of buildings.

In Figure 4 we show a high-level block diagram of the proposed workflow. Several optical images available at different dates are processed independently to generate maps of candidate BBFs. The whole multi-temporal SAR stack is instead processed jointly to produce the built-up areas mask. These outputs are then converted in a vectorial form and processed in the GIS environment, together with the cadastral map including prior information on the location of facilities officially registered. The final product is a map of likely BBFs unknown to the official registry, which can be used in turn as input for on-site inspections by the environment protection and law enforcement agencies.

In Figure 5 we show finer details for the optical and SAR processing chains. The main goal of optical image processing is classification: based on their properties, pixels are labeled as either "manure" or "not manure". To improve performance and reduce complexity, classification is carried out on homogeneous image segments rather than isolated pixels. Therefore, after a preliminary pansharpening, the image is segmented, in order to identify its elementary homogeneous regions. Each high-resolution segment is then characterized by its spectral signature and classified.

The SAR image processing block, instead, provides a map of the urban areas in the scene. This is obtained by first co-registering the SAR images to a common master, and then computing the stack of corresponding coherence maps which is thresholded to provide the desired urban mask.

In the data fusion block (see Figure 4), after geo-referencing and co-registering

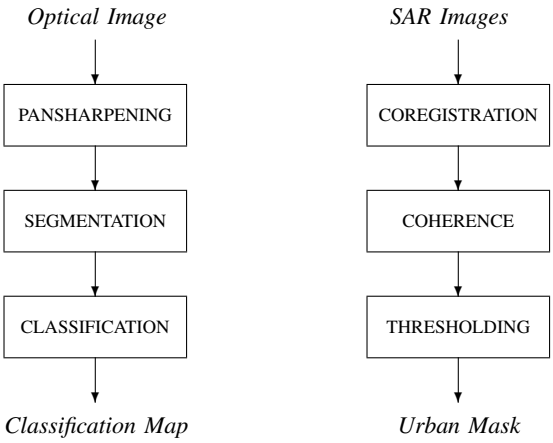

Figure 5. Optical-domain and SAR-domain detailed processing chain.

all products, the classification maps corresponding to the various dates (two in our case) are combined through a logical AND, discarding in advance, however, regions too small and isolated. Detections occurring in urban areas, singled out thanks to the SAR-domain processing, are removed as well. The resulting map, converted from raster to vectorial form, is eventually compared with the cadastral map to find suspect BBFs. Despite its simplicity, this workflow turns out to be quite effective, as shown in Section 7, and easily manageable by nonexpert users, as the operators of governmental agencies may be expected to be. In fact, the output BBFs map can be obtained and updated with a small number of simple operations, making the human-machine interaction experience quick and comfortable, thus oriented towards the end-users community (Madhok and Landgrebe 2002; Gaetano et al. 2014a; Amitrano et al. 2015).

4. Optical-domain Image Processing

The first task carried out on the multiresolution images is pan-sharpening, which provides a data cube with full spatial and spectral resolution. We resort here to the Gram-Schmidt method, which has become very popular for pan-sharpening (Laben and Brower 200) due to its good performance over a wide variety of applications (Du et al. 2007; Yusuf et al. 2012). Moreover, it is implemented in the ENVI package, one of the most commonly used commercial software packages for the processing of remote-sensing images. In the following, the segmentation and classification processing are discussed.

4.1 *Segmentation*

Remote-sensing images come in the form of arrays of pixels, hardly a good basis on which to make reliable decisions. Therefore, it is convenient to raise the description to a higher level, by identifying elementary regions, or segments, which are internally homogeneous, and hence characterized by means of a few compact features. These are, however, large enough to simplify all subsequent processing and enable the fast and reliable achievement of all application goals. This processing paradigm is also referred to as object-based image analysis (OBIA) or geospa-

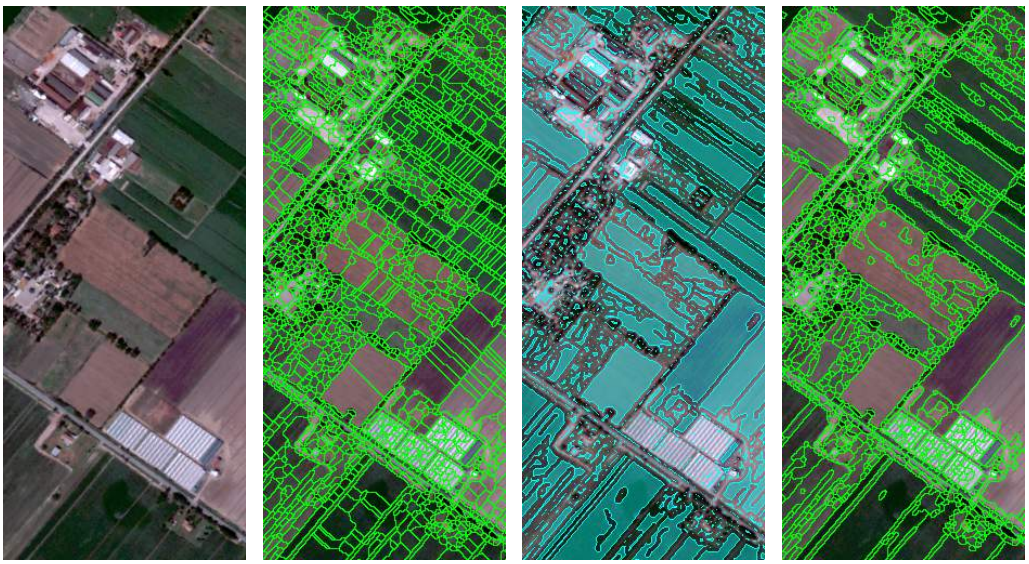

(a) (b) (c) (d)

Figure 6. Edge Mark and Fill segmentation. (a) original RGB clip (about 540 × 200 m^2), (b) watershed segmentation map, (c) morphological and spectral markers, (d) EMF segmentation map.

tial OBIA (GEOBIA), and is widely adopted as shown in the review proposed in Blaschke (2010).

In the present study, given the need to extract region contours as accurately as possible for subsequent vectorization, we resort to edge-oriented segmentation techniques based on the watershed transform. First, we compute the map of image edges on the high-resolution panchromatic component.

However, the application of watershed to real-world remote sensing images, see Figure 6(a), provides an exceedingly large number of regions, Figure 6(b), many of which are due to minor imperfections of the edge map, or just to the discrete geometry of the images and should be obviously merged together. We therefore apply a more sophisticated segmentation algorithm, called Edge Mark and Fill (EMF), proposed originally in (Gaetano et al. 2012) and generalized in (Gaetano et al. 2014b) for color and multiresolution images. Edge detection is here performed using the Canny edge detector (Canny 1986), which is largely available and flexible and has been proven to perform well within the EMF framework.

EMF carries out a marker-controlled watershed segmentation. Markers are regions superimposed to the original image that force all pixels covered by a given mark to belong to the same segment. They can be put manually by an operator, a tedious and low-precision task or, more interestingly, through some specific automatic procedure, e.g. (Xiao et al. 2007; Gaetano et al. 2012). In EMF, two types of markers are automatically generated and fused, based, respectively, on the morphological properties of the Canny edge map, and on the spectral properties of the corresponding adjacent regions. In Figure 6(c), we show some of the markers generated by EMF, superimposed on the original image. Thanks to such markers, the final segmentation map, shown in part (d), comprises a much smaller number of segments with the same accuracy, partially closing the gap with the ideal map that a human being might generate.

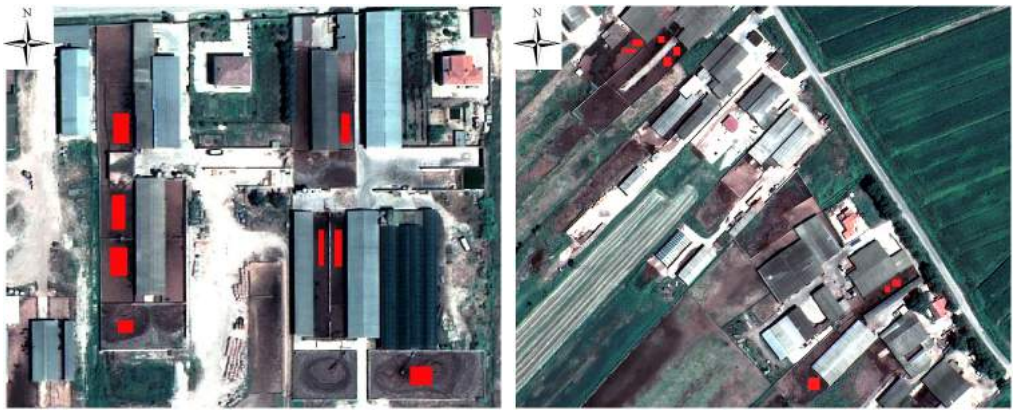

Figure 7. Training (left) and test (right) sets for classification. Red boxes correspond to "manure" areas.

4.2 *Spectral Classification*

Our aim is to classify each segment of the area of interest as either "manure" or "not manure", based on the spectral response vectors of the component pixels, obtained through the pansharpening of the multiresolution optical image. To this end, given the wealth of information available, we resort to *supervised* classification.

The spectral response of "manure" cannot be discriminated from that of other semantic classes, and hence a more general "wet soil" class was used with regard to classification. As discussed in the following, "manure" can be discriminated with respect to other land covers of the "wet soil" spectral class only by going beyond spectral analysis. The proposed model eventually comprises 15 classes (see Table 2), including for example "green vegetation", "dry vegetation", and "bare soil". For our purposes, however, all segments not classified as "wet soil" are eventually collected in a single class and discarded from further analysis.

A relatively small fraction of the image was selected as the training set, taking care to include all the features of interest. More precisely, for each class of interest, we selected from 20 to 50 segments each comprising a few hundreds pixels, except for some classes of particularly small objects, such as clay, asphalt, green roofs, and trees. In fact for these classes smaller ground truth segments are needed (fewer than 100 pixels) for reliable annotation. Overall, about 200,000 pixels were used for the training set. In the same manner, we formed a test set of approximately 110,000 pixels, taking care to avoid any intersection between training set and test set segments. Figure 7(a) shows some "wet soil" training set segments (to avoid cluttering the figure, segments of other classes are not shown), while Figure 7(b) shows some test set segments of the same class.

Given this detailed 15-class model, it is reasonable to characterize each class $c = 1, \ldots, C$ through a single-mode probability density function (pdf), and in particular, a multivariate Gaussian with mean μ_c and covariance matrix Σ_c. These synthetic statistics are maximum-likelihood estimated based on the training data, with high reliability, given the low-dimensionality (four) of the vector space, much smaller than the number of available pixels per class.

Given the spectral vector $X(s) = x$ associated with pixel s, the label or class $\widehat{c}(s) \in \mathcal{C} = 1, 2, \ldots, C$ is chosen according to the MAP (Maximum A-posteriori Probability) rule. However, lacking any prior information on the classes, this reduces to the maximum likelihood rule, and eventually, for the assumed Gaussian statistics, to

$$\widehat{c}(s) = \arg\min_{c \in \mathcal{C}} \left[\ln |\Sigma_c| + (x - \mu_c)^T {\Sigma_c}^{-1} (x - \mu_c) \right] \tag{1}$$

To reduce the influence of noise, the decision is made on segments, rather than pixels. For each homogeneous region singled out by segmentation, the average spectral signature is computed and used for classification. Segmentation granularity is kept high in order to preserve the homogeneity of the spectral response in the same segment. As a consequence, the physical objects of the scene are often composed by several segments. Because of the use of segments rather than pixels, the classification appears to be fairly reliable, despite the simple multivariate Gaussian model adopted.

5. SAR-domain Image Processing

The goal of SAR-domain processing is to extract a pixel-based map of urban areas, through the analysis of interferometric coherence. To this end, SAR images are preliminarily coregistered with one-another by a three-step procedure (Li and Bethel 2008) during which the alignment is progressively refined, first using orbit information, then the cross-correlation between coupled windows, and finally optimizing results with Powell's method.

Man-made areas can be separated from natural ones based on the interferometric coherence between successive acquisitions, because of their different scattering formation physical principles (Rosen et al. 2000). Indeed, in man-made areas the back-scattering is dominated by the multiple reflections between the building elements and the ground. Moreover, double and triple reflections due to the dihedrals and trihedrals are stable also with respect to variations in the observation geometry (Ferretti et al. 2007). Rural areas, typically composed of trees, cultivated fields, grasses and crops, exhibit instead back-scattering values that are strongly influenced by the observation geometry as well as by changes in the scene. This causes low values of interferometric coherence, especially if it is computed with a large temporal baseline. Of course, the typical time lapse necessary to cause an appreciable fall of the coherence is different for each of the above cited objects and depends also on the season (for example, a single rainfall can change the scene characteristics with a dramatic reduction of the coherence between the pre-event and post-event images) (Franceschetti et al. 2003).

In the available dataset, the average interval between two acquisitions is in the order of one month, which is sufficient for assuming that only stable targets (such as buildings and roads) exhibit a high level of interferometric coherence. However, in order to minimize the probability of false alarms, a mean coherence map was generated by averaging all the coherence maps between an image assumed as reference and all others. Figure 8 represents the mean coherence values (left) and map (right) of the whole SAR scene under analysis, projected onto the WGS84 geographic coordinate system (north at top), where the sea has been manually removed since it is irrelevant to the analysis conducted in this work. Note that to obtain the binary map, man-made and natural areas are separated by simple thresholding (Gaetano et al. 2014a).

As a final step, we go from pixel-level to region-level maps, based on prior information. Indeed, urban zones are areas of significant spatial extension with a high-density of man-made structures. Following this definition, we first compute local density by averaging the pixel-level map in a circular region of radius 200 pixel (600 m) centered on the target. Then the density map is thresholded, and small (less than 10000 pixels) isolated regions are removed. Eventually, only high density large regions are classified as urban areas. Figure 9 depicts the full pan-sharpened data set available. The highlighted portion (in yellow) overlaps the co-registered

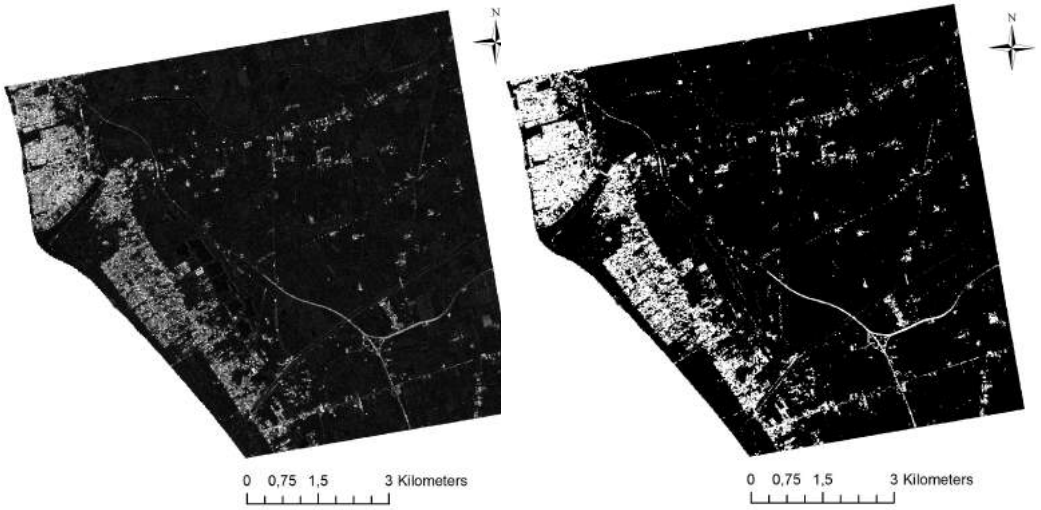

Figure 8. Geocoded mean coherence map (left) and corresponding man-made mask (right). Bright pixels indicate mostly man-made structures.

Figure 9. Dense urban areas (in lilac) extracted by refining the man-made map, superimposed on the RGB composite image.

SAR multitemporal data and is hence used in this work.

6. Data fusion

In the data fusion block, decisions are made based on all available pieces of information. Before that, however, co-registration and rectification are required, in order to provide coherent data.

6.1 *Coregistration between SAR and optical images*

SAR/optical image registration aims at correcting the misalignment of geocoded SAR with respect to the rectified optical images. The SAR geocoded images were obtained via a range-Doppler mode, with a 20 m-resolution digital elevation model (DEM) for compensation of terrain-induced distortion.

Although many automatic registration techniques have been proposed in the lit-

erature (*e.g.,* (Inglada and Giros 2004; Suri and Reinartz 2010; Fan et al. 2013)), their robustness is still limited. Therefore, we refined the SAR/optical alignment with user-defined Ground Control Points (GCPs), whose selection is time consuming and influenced by the operator sensitivity, but must be performed only once for the whole dataset.

In order to improve the accuracy of the GCPs identification in the SAR maps, a multitemporal De Grandi filter has been applied to the entire available dataset, in order to reduce the effects of speckle without loss of spatial resolution, followed by nonlocal spatial despeckling (Parrilli et al. 2012). Then, the selection of GCPs was based on the identification of points that are easily recognizable and detectable in both the SAR and optical maps, despite their different geometries. Hence, the point candidate to be selected as GCPs should be relative to areas which are stable in amplitude (on the SAR map) and easily separable from surrounding regions (Zitova and Flusser 2003), such as road crossings, buildings, boundaries between homogeneous areas, or other dominant features observable in both images.

Thirty uniformly distributed GCPs were selected for building the warp polynomial needed to align the SAR to the optical reference image. This processing allowed an alignment in the order of pixel size, which is consistent with the project objectives.

6.2 *Rectification based on a DEM*

Often georeferencing is not sufficient to guarantee a precise spatial correspondence among physical regions and objects in the various images, even when DEMs are used for either orthorectification or geocoding. To improve the geometric quality of the original images, rectification was applied using the rational function model (RFM) (Tao and Hu 2000), adopted with success in many applications (e.g. Maglione, Parente, and Vallario (2014)). This approach requires a DEM of the whole area and at least 39 GCPs with known image coordinates and 3D (altimetric and planimetric) position in a geodetic-cartographic reference system. A 5m$\times$5m DEM of the region of interest was built by means of linear interpolation on vector maps at a scale of 1:5000, with 99 GCPs for the first image and 201 for the second. Accuracy was tested by considering the difference between the exact and estimated coordinates, by means of root mean squared error (RMSE = $\sqrt{\text{MSE}}$). RMSE turned out always to be below 1 m for GCPs, and slightly higher than that for a disjoint set of control points.

6.3 *Decision*

After co-registering all products, several simple decision rules can be enacted based on the segment-level classification of optical images and on the urban mask. In particular, we show results obtained using only one or both of the optical images and with and without urban masking. When two images are used, only segments detected in both are taken into account (hence, a more conservative choice). Moreover, the urban mask, when used, allows one to discard segments detected in urban areas. A more detailed description of the decision process is deferred to the next section, in the context of the experimental analysis.

7. Experimental results

Here we report results of experiments carried out to validate the proposed algorithm. We will analyze separately the performance of classification and detection tasks. However, since in both cases we are eventually interested in detecting the presence of a given target class, "manure" in classification, and "buffalo breeding facility" in detection, we will consider always the same measures, used in two-class hypotheses tests, namely precision P and recall R, and the synthetic F_1 measure F. These measures are defined, w.r.t, a generic target class T, as

$$P = \Pr(c = T \mid \widehat{c} = T) \tag{2}$$

$$R = \Pr(\widehat{c} = T \mid c = T) \tag{3}$$

and

$$F = \frac{2PR}{P + R} \tag{4}$$

where PR denotes probability, and c and $\widehat{c}$ indicate the true and selected class/hypothesis. A high precision indicates that when the target class is detected, the decision is very likely correct. A high recall indicates that when the target class is present, it will be very likely detected. Therefore, both measures are desired to be large, and by tuning the classification parameters one may increase one of them but decrease the other. A synthetic measure of performance is the F-measure, a harmonic mean of precision and recall, which is large only when one or both indicators are rapidly reducing in value.

7.1 *Classification*

Our classifier is trained on *pixels* drawn from the training set, while the decision is made on *segments*, namely on the average spectral response computed over all pixels belonging to a segment. This mixed solution was chosen after comparing performance with the other meaningful alternatives, where training and classification are performed both on pixels or both on segments. Results are reported in Table 1, w.r.t. the target class "wet soil", and are computed pixel-based irrespective of how the decision is made. Although the performance is definitely good in all cases, the selected mixed solution guarantees an appreciable gain in precision, and therefore in the F-measure. Indeed, when decisions are made on individual pixels, the influence of noise is more relevant, causing a drop in both precision and recall. In the third case, instead, the problem is likely the limited number of segments available for training, which reduces the ability of the classifier to deal with outliers of other classes. We underline also that the pixel-based solution must be excluded not only for its inferior performance, but also because we will use segments as the basis for the detection of BBFs.

For the selected solution, we computed the complete 15-class confusion matrix A over a total of N=113367 pixels, with entries a_{ij} counting the number of pixels of class j that have been classified as belonging to class i. Based on a confusion matrix, several global quality indicators are usually computed. The *overall accuracy*

training	classification	precision	recall	F-measure
pixel	pixel	0.862	0.975	0.915
pixel	segment	0.902	0.995	0.946
segment	segment	0.854	0.994	0.919

Table 1. Comparison of training/cassification combinations.

τ, defined as

$$\tau = \sum_i a_{ii}/N \tag{5}$$

is the percentage of sample pixels that are correctly classified. The *Kappa parameter*, defined as

$$\kappa = \frac{N\sum_i a_{ii} - \sum_i a_{i+}a_{+i}}{N^2 - \sum_i a_{i+}a_{+i}} \tag{6}$$

with $a_{i+} = \sum_j a_{ij}$ and $a_{+i} = \sum_j a_{ji}$, discounts successes obtained by chance, and is therefore more conservative (it can be also negative). The average accuracy (AA), also frequently used, is defined as the mean of per-class *producer's accuracies* a_{ii}/a_{+i}. Finally, the normalized accuracy τ^{norm} is computed on a confusion matrix modified as described in Congalton (1991) in order to give equal importance to all classes, irrespective of the number of samples in each one. These indexes are all very high for our classifier: $\tau = 78.19\%, \kappa = 76.05\%, AA = 80.98\%, \tau^{norm} = 86.92\%$, especially considering the large number of classes considered, some of which pretty similar to one another.

	1	**2**	**3**	**4**	**5**	**6**	**7**	**8**	**9**	**10**	**11**	**12**	**13**	**14**	**15**	Σ
1	9712	2502	89													1233
2	42	4764														4806
3	76	86	1450		4	71	174		541	982	16					3400
4	4	8	3	593						2						610
5			62		4788	3		6		10					163	5432
6			18			9779	311	3	311	161					35	10618
7						79	3026									3105
8						5	1	1991							402	2399
9			609			15191		9	848	1						16658
10			1203		5	17			542	7203	2				11	8983
11	265		14		41	57			3	18	1402		616	47	42	2505
12	433											14417	17			14867
13												60	4214	574		4848
14			18			165			6	159	130	109	153	11199	67	12006
15			5		48	144		49		2					10939	11187
Σ	10532	7360	3471	593	4886	25511	3512	2058	2251	8538	1550	14586	5000	11820	11659	

Table 2. 15-class confusion matrix. Labels: 1=Shallow Water, 2=Deep Water, 3=Asphalt, 4=Pools, 5=Rock, 6=Bare Soil, 7=Wet Soil, 8=Clay Roofs, 9=Asphalt Roofs, 10=Metal Roofs, 11=Green Roofs, 12=Trees, 13=Grass, 14=Sparse Vegetation, 15=Dry Vegetation.

In Table 2 we report the confusion matrix. With perfect classification, only di-

Figure 10. The image used in the experiments. Performance is computed on the large region in the yellow box. The small region in the red box is used for detailed visual inspection of results.

Figure 11. Segment-level decisions on the same small area of the image at the two dates. Green=correct, red: false alarm.

agonal entries should be larger than 0, and indeed, most off-diagonal entries are 0 (blank) or very close to it. In any case, we are especially interested in the "wet soil" class, number 7, including "manure", for which both producer's and user's accuracy are clearly very high.

7.2 *Detection*

Detection performance is assessed on a large part of the available image, shown in the yellow box of Figure 10, while the small region in the red box will be used only for visual inspection. Measuring performance is less obvious in this case. Our goal is to detect BBFs, when present, and to avoid declaring their presence otherwise. First, to measure success in the first task, we need a ground truth which identifies all such facilities in the test area. Therefore, an expert photointerpreter (the first author of this work) analyzed thoroughly the whole image and, based also on other complementary sources of information, detected eventually 76 BBFs, drawing their approximate contours in GIS as regular polygons, shown in yellow (nine of them) in the example clip of Figure 11.

This figure also shows the segments classified as "wet soil", in green (correct decision) when more than 50% of the segment is inside a BBF, or in red (false

variant	images	urban mask	precision	recall	F-measure
1	T_1	NO	0.973	0.154	0.266
2	T_1		0.986	0.234	0.379
3	$T_1 + T_2$		0.934	0.862	0.897
4	T_1	YES	0.973	0.272	0.425
5	T_1		0.986	0.426	0.596
6	$T_1 + T_2$		0.934	0.949	0.941

Table 3. Detection performance with different variants of the proposed procedure.

alarm) otherwise. However, we are interested in detecting facilities, not segments. Therefore, we use these data to label the 76 BBFs as either detected (when comprising at least one green segment) or missed (when no green segment falls within its bounding polygon). In the example clip, all nine BBFs are detected at both dates. With this information, we can compute a meaningful recall indicator. In regard to precision, no similar conversion seems possible. So we are forced to operate at segment level, computing precision as the ratio between the number of segments (green) correctly declared "wet soil", possibly manure, and the number of all segments (green or red) declared "wet soil", irrespective of their real class, thus including errors. Although working at segment level, this latter indicator provides a good insight into the quality of the whole procedure. If precision is too low, the technique indicates many more targets than actually present, becoming basically useless. To reduce false alarms we resort to the urban mask of Figure 9, computed from the SAR coherence map.

In Table 3 we report the performance indicators obtained using all pieces of information available (last row) or just some of them. In the first two cases, only one of the optical images is used, either T_1 or T_2. In both cases almost all BBFs are detected (high precision), but also thousands of "manure" regions unrelated with BBFs (low recall) resulting in an acceptable overall performance, as testified by the very low F-measure value. This was to be expected from the analysis of Figure 11, where many red segments appear. However, while regions in BBFs are persistent, because they are continuously covered by manure, external regions are only occasionally classified as such, maybe because periodically fertilized, and can be eliminated through a multitemporal analysis. By combining the maps relative to both time instances through a simple logical AND (case 3), a much better recall is obtained. However, although not in the example clip, some BBFs are lost due to the logical AND, reducing slightly precision. Despite this loss a much higher F-measure is observed. Figure 12 shows the effects of the logical AND on our example clip. In the last three rows of the table we report the same data as before when the mask for dense urban areas, derived from SAR images, is also used. This mask allows us to reject a number of bare soil areas that, when shadowed by buildings, are spectrally indistinguishable by wet soil, generating a large number of false alarms. Therefore, recall increases significantly with respect to the corresponding cases without urban mask, while precision is obviously not affected by masking, because BBFs are always rather far from large urban centers. The full fledged technique (case 6) guarantees eventually both high precision, with 71 facilities detected out of 76, and high recall, with only 30 false alarm segments out of 590.

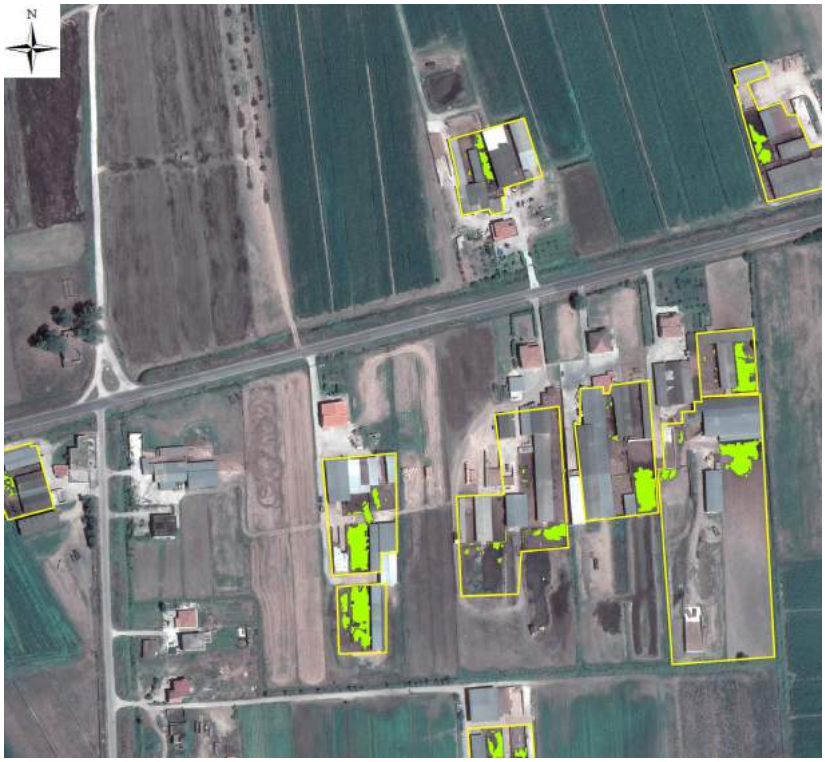

Figure 12. Segment-level decisions based on multitemporal data. No false alarm occurs in the clip.

8. Conclusions and future research

We have proposed a methodology for detecting small buffalo-breeding facilities based on multi-sensor and multitemporal remote-sensing data and GIS-based processing. The performance of the proposed system is quite satisfactory with an F-measure always above 0.9. Hence, it can be a valuable tool for monitoring environmental hazards, adaptable to different tasks by modifying the input data, and also in regard to various highly data-dependent processing tasks, such as denoising or segmentation. For example, work is under way to adapt the tool to the detect illegal landfill.

Of course, there is room for further improvement under several points of view. First of all, with more images available, a better decision strategy could be implemented, so as to detect *all* areas of interest with limited false alarms. However, even with the data currently available, performance could be improved by better exploiting information available in the GIS, such as the position of candidate areas w.r.t. the road network and waterways, or other geographic layers coming from different sources. Work is currently under way to investigate these issues.

References

Ali, I., C. Schuster, M. Zebisch, M. Forster, B. Kleinschmit, and C. Notarnicola. 2013. "First Results of Monitoring Nature Conservation Sites in Alpine Region by Using Very High Resolution (VHR) X-Band SAR Data." *IEEE Journal of Selected Topics in Applied Earth Observations and Remote Sensing* 6 (5): 2265–2274.

Amitrano, D., G. Di Martino, A. Iodice, D. Riccio, and G. Ruello. 2015. "A new framework for SAR multitemporal data RGB representation: rationale and products." *IEEE Transactions on Geoscience and Remote Sensing* 53 (1): 117–133.

Amitrano, D., G. Di Martino, A. Iodice, D. Riccio, G. Ruello, F. Ciervo, M. N. Papa, and Y. Koussoubé. 2014. "Effectiveness of High-Resolution SAR for Water Resource Management in Low-Income Semi-Arid Countries." *International Journal of Remote Sensing* 35 (1): 70–88.

Barba, M., A. Mazza, C. Guerriero, M. Di Maio, F. Romeo, P. Maranta, I. Marino, M. G. Paggi, and A. Giordano. 2011. "Wasting Lives: The Effects of Toxic Waste Exposure on Health. the Case of Campania, Southern Italy." *Cancer Biology & Therapy* 12 (2): 106–111.

Blaschke, T. 2010. "Object based image analysis for remote sensing." *ISPRS Journal of Photogrammetry and Remote Sensing* 65 (1): 2–16.

Brilis, G.M., R.J. van Waasbergen, P.M. Stokely, and C.L. Gerlach. 2001. "Remote sensing tools assist in environmental forensics: Part II - Digital Tools." *Environmental Forensics* 2 (3): 223 – 229.

Canny, J. 1986. "A Computational approach to edge detection." *IEEE Transactions on Pattern Analysis and Machine Intelligence* 8 (6): 679–698.

Congalton, R. G. 1991. "A Review of Assessing the Accuracy of Classifications of Remotely Sensed Data." *Remote Sensing of Environment* 37 (1): 35–46.

De Grandi, G. F., M. Laysen, J.-S. Lee, and D. Schuler. 1997. "Radar reflectivity estimation using multiple SAR scenes of the same target: technique and applications." In *IEEE International Geoscience and Remote Sensing Symposium,* 1047–1050. August.

Deledalle, C.-A., L. Denis, G. Poggi, F. Tupin, , and L. Verdoliva. 2014. "Exploiting Patch Similarity for SAR Image Processing: The Nonlocal Paradigm." *IEEE Signal Processing Magazine* 31 (4): 69–78.

Du, Q., N. H. Younan, R. King, , and V. P. Shah. 2007. "On the Performance Evaluation of Pan-Sharpening Techniques." *IEEE Geoscience and Remote Sensing Letters* 4 (4): 518–522.

EPA, U.S. 2011. "National pollutant discharge elimination system (NPDES) concentrated animal feeding operation (CAFO) reporting rule." .

Esposito, M., F. P. Serpe, F. Neugebauer, S. Cavallo, P. Gallo, G. Colarusso, L. Baldi, G. Iovane, and L. Serpe. 2010. "Contamination Levels and Congener Distribution of PCDDs, PCDFs and Dioxin-Like PCBs in Buffalo's Milk from Caserta Province (Italy)." *Chemosphere* 79 (3): 341–348.

Faisal, K., M. Alahmad, and A. Shake. 2012. "Remote Sensing Techniques as a tool for Environmental Monitoring." In *International Archives of the Photogrammetry, Remote Sensing and Spatial Iinformation Sciences (XXII ISPRS Congress),* 513 – 518. August.

Fan, B., C. Huo, C. Pan, and Q. Kong. 2013. "Registration of optical and SAR satellite images by exploring the spatial relationship of the improved SIFT." *IEEE Geoscience and Remote Sensing Letters* 10 (4): 657–660.

Fatta-Kassinosa, D., I. K. Kalavrouziotisb, P. H. Koukoulakisc, and M. I. Vasqueza. 2011. "The Risks Associated with Wastewater Reuse and Xenobiotics in the Agroecological Environment." *Environmental Health Perspectives* 409 (19): 3555–3563.

Ferretti, A., A. Monti-Guarnieri, C. Prati, F. Rocca, and D. Massonnet. 2007. *InSAR principles: guidelines for SAR interferometry processing and interpretation.* Postbus 229, 2200 AG Noordwijk: ESA Publications, ESTEC.

Fontanelli, G., A. Crema, R. Azar, D. Stroppiana, P. Villa, and M. Boschetti. 2014. "Crop Mapping Using Optical and SAR Multi-Temporal Seasonal Data: A Case Study in Lombardy Region, Italy." In *IEEE International Geoscience and Remote Sensing Symposium,* 1489–1492.

Franceschetti, G., A. Iodice, D. Riccio, G. Ruello, , and S. Cimmino. 2003. "SAR Raw Signal Simulation for Urban Structures." *IEEE Transactions on Geoscience and Remote Sensing* 41 (9): 1986–1995.

Gaetano, R., D. Amitrano, G. Masi, G. Poggi, G. Ruello, L. Verdoliva, and G. Scarpa. 2014a. "Exploration of multitemporal COSMO-SkyMed data via tree-structured MRF segmentation." *IEEE Journal of Selected Topics in Applied Earth Observations and Remote Sensing* 7 (7): 2763–2775.

Gaetano, R., G. Masi, G. Poggi, L. Verdoliva, and G. Scarpa. 2014b. "Marker controlled

watershed based segmentation of multi-resolution remote sensing images." *IEEE Transactions on Geoscience and Remote Sensing* in press.

Gaetano, R., G. Masi, G. Scarpa, and G. Poggi. 2012. "A marker-controlled watershed segmentation: Edge, mark and fill." In *IEEE International Geoscience and Remote Sensing Symposium,* 4315–4318. july.

Gao, M., S. Liu, Z. Qin, J. Qiu, B. Xu, W. Li, X. Yang, and J. Li. 2013. "Integration of remote sensing with GIS for grassland snow cover monitoring and snow disaster evaluating in Tibet." In *proc. of SPIE, Remote Sensing for Environmental Monitoring, GIS Applications, and Geology VIII,* Vol. 7110October.

Gerba, C. P., and J. E. Smith. 2005. "Sources of Pathogenic Microorganisms and Their Fate during Land Application of Wastes." *Journal of Environmental Quality* 34 (1): 42–48.

Horrigan, L., R. S. Lawrence, and P. Walker. 2002. "How Sustainable Agriculture Can Address the Environmental and Human Health Harms of Industrial Agriculture." *Environmental Health Perspectives* 10 (5): 445–456.

Im, J., J.R. Jensen, R.R. Jensen, J. Gladden, J. Waugh, and M. Serrato. 2007. "Vegetation cover analysis of hazardous waste sites in Utah and Arizona using hyperspectral remote sensing." *Remote Sensing* 4: 327 – 353.

Infascelli, R., S. Faugno, S. Pindozzi, R. Pelorosso, and L. Boccia. 2010. "The Environmental Impact of Buffalo Manure in Areas Specialized in Mozzarella Production, Southern Italy." *Geospatial Health* 5 (1): 131–137.

Inglada, J., and A. Giros. 2004. "On the possibility of automatic multisensor image registration." *IEEE Transactions on Geoscience and Remote Sensing* 42 (10): 2104–2120.

Jensen, J., M. Hodgson, M. Garcia-Quijano, J. Im, and J. Tullis. 2009. "A remote sensing and GIS-assisted spatial decision support system for hazardous waste site monitoring." *Photogrammetric Engineering and Remote Sensing* 75 (2): 169 – 177.

Jongbloed, A. W., and N. P. Lenis. 1998. "Environmental Concerns about Animal Manure." *Journal of Animal Science* 76 (10): 2641–2648.

Karathanassi, V., C. Choussiafis, and Z. Grammatikou. 2012. "Monitoring the change in volume of waste in landfill using SAR interferometry." In *32nd EARSel Symposium, Adavances in Geosciences,* 540 – 551.

Laben, C. A., and B. V. Brower. 200. "Process for Enhancing the Spatial Resolution of Multispectral Imagery Using Pan-Sharpening." US Patent 6,011,875.

Lega, M., D. Ceglie, G. Persechino, C. Ferrara, and R.M.A. Napoli. 2012a. "Illegal dumping investigation: A new challenge for forensic environmental engineering." *WIT Transactions on Ecology and the Environment* 163: 3–11.

Lega, M., J. Kosmatka, C. Ferrara, F. Russo, R. M. A. Napoli, and G. Persechino. 2012b. "Using advanced aerial platforms and infrared thermography to track environmental contamination." *Environmental Forensics* 13 (4): 332–338.

Lega, M., and R. M. A. Napoli. 2010. "Aerial infrared thermography in the surface waters contamination monitoring." *Desalination and Water Treatment* 23 (1-3): 141–151.

Lein, J.K. 2013. "Landfill monitoring using remote sensing: a case study of Glina, Romania." *Waste Management and Research* 31: 1075 – 1080.

Li, Z., and J. Bethel. 2008. "Image coregistration in SAR interferometry." In *The International Archives of the Photogrammetry, Remote Sensing and Spatial Information Services, XXXVII (B1),* 433–438.

Madhok, V., and D. A. Landgrebe. 2002. "A process model for remote sensing data analysis." *IEEE Transactions on Geoscience and Remote Sensing* 40 (3): 680–686.

Maglione, P., C. Parente, and A. Vallario. 2014. "Coastline Extraction Using High Resolution WorldView-2 Satellite Imagery." *European Journal of Remote Sensing* 47: 685–699.

Menzi, H., O. Oenema, C. Burton, O. Shipin, P. Gerber, T. Robinson, and G. Franceschini. 2010. "Impacts of Intensive Livestock Production and Manure Management on the Environment." In *Livestock in a Changing Landscape: Drivers, Consequences and Responses,* edited by H. Steinfeld, H. Mooney, L. E. Neville, and F. Schneider. Washington, DC: Island Press.

Ottavianelli, G., S. Hobbs, R. Smith, and D. Bruno. 2005. "Assessment of SAR data and

interferometric products for solid waste landfill management." In *RSPSoc Annual Conference 2005 - Measuring, Mapping and Managing a Hazardous World,* 1–8. September.

Parrilli, S., M.Poderico, C.V.Angelino, and L.Verdoliva. 2012. "A nonlocal SAR image denoising algorithm based on LLMMSE wavelet shrinkage." *IEEE Transactions on Geoscience and Remote Sensing* 50 (2): 606–616.

Persechino, G., M. Lega, G. Romano, F. Gargiulo, and L. Cicala. 2013. "IDES project: An advanced tool to investigate illegal dumping." *WIT Transactions on Ecology and the Environment* 173: 603–614.

Pohl, C., and J. V. Genderen. 1998. "Multisensor image fusion in remote sensing: concepts, methods and applications." *International Journal of Remote Sensing* 19 (5): 823–854.

Pringle, J.K., A. Ruffell, J.R. Jervis, L. Donnelly, J. McKinley, J. Hansen, R. Morgan, D. Pirrie, and M. Harrison. 2012. "The use of geoscience methods for terrestrial forensic searches." *Earth-Science Reviews* 114: 108–123.

Rosen, P. A., S. Hensley, I. R. Joughin, F. K. Li, S. N. Madsen, E. Rodriguez, and R. M. Goldstein. 2000. "Synthetic Aperture Radar Interferometry." *Proceedings of the IEEE* 3 (88): 333–382.

Silvestri, S., and M. Omri. 2008. "A method for the remote sensing identification of uncontrolled landfills: formulation and validation." *International Journal of Remote Sensing* 29: 975–989.

Slonecker, T., G.B. Fisher, D.P. Aiello, and B. Haack. 2010. "Visible and infrared remote imaging of hazardous waste: a review." *Remote Sensing* 2: 2474 – 2508.

Solberg, A.H.A., T. Taxt, and A.K. Jain. 1996. "A Markov random field model for classification of multisource satellite imagery." *IEEE Transactions on Geoscience and Remote Sensing* 34 (1): 100–113.

Suri, S., and P. Reinartz. 2010. "Mutual-information-based registration of Terrasar-X and Ikonos imagery in urban areas." *IEEE Transactions on Geoscience and Remote Sensing* 48 (2): 939–949.

Tao, C. V., and Y. Hu. 2000. "Image rectification using a generic sensor model - rational function model." In *International Archives of Photogrammetry and Remote Sensing, Vol. XXXIII, Part B3,* 874–881.

Triassi, M., R. Alfano, M. Illario, A. Nardone, O. Caporale, , and P. Montuori. 2015. "Environmental Pollution from Illegal Waste Disposal and Health Effects: A Review on the Triangle of Death." *International Journal of Environmental Research and Public Health* 12 (2): 1216–1236.

Waske, B., and S. van der Linden. 2008. "Classifying multilevel imagery from SAR and optical sensors by decision fusion." *IEEE Transactions on Geoscience and Remote Sensing* 46 (5): 1457–1466.

Weis, M., S. Müller, C.-E. Liedtke, and M. Pahl. 2005. "A framework for GIS and imagery data fusion in support of cartographic updating." *Information Fusion* 6 (4): 311–317.

Weng, Q. 2002. "Land use change analysis in the Zhujiang Delta of China using satellite remote sensing, GIS and stochastic modelling." *Journal of Environmental Management* 64: 273–284.

Xiao, P., X. Feng, S. Zhao, and J. She. 2007. "Multispectral IKONOS image segmentation based on texture marker-controlled watershed algorithm." In *Proc. SPIE: Remote Sensing and GIS Data Processing and Applications; and Innovative Multispectral Technology and Applications,* Vol. 6790.

Yusuf, Y., I. Alimuddin, J. T. S. Sumantyo, , and H. Kuze. 2012. "Assessment of Pan-Sharpening Methods Applied to Image Fusion of Remotely Sensed Multi-Band Data." *International Journal of Applied Earth Observation and Geoinformation* 18: 165–175.

Zhang, J. 2010. "Multi-source remote sensing data fusion: status and trends." *International Journal of Image and Data Fusion* 1 (1): 5–24.

Zitova, B., and J. Flusser. 2003. "Image registration methods: a survey." *Image and Vision Computing* 21 (11): 977–1000.